Full length article

Microstructure and mechanical properties of Ti-Al-Cr-N films: Effect of current of additional anode

Ying Kong[a], Xiubo Tian[a,*], Chunzhi Gong[a], Qinwen Tian[a], Detao Yang[a], Mingzhong Wu[b], Muqin Li[b], Dmitriy A. Golosov[c]

[a] State Key Laboratory of Advanced Welding and Joining, Harbin Institute of Technology, Harbin 150001, China
[b] School of Materials Science & Engineering, Jiamusi University, Jiamusi 154007, China
[c] Thin Film Research Laboratory, Belarusian State University of Informatics and Radioelectronics, Minsk, Belarus

ABSTRACT

Ti-Al-Cr-N films were fabricated on the surface of Si (100) wafers and M2 high speed steel by electrically enhanced discharge cathodic arc technology. The effect of the current of additional anode on plasma discharge, microstructure, hardness and adhesion strength has been investigated systematically. The results show that the discharge of additional anode can improve substrate current distinctly and mainly affects the excitation and ionization of nitrogen, rather than that of metal. Besides, the enhanced discharge can increase the ratio of substrate ion current to thickness of films (E_{bi}). The Ti-Al-Cr-N film deposited at the current of additional anode of 30 A possesses the highest nanohardness (31.3 GPa), the best adhesion strength between film and substrate (HF1), and the maximum H/E^* and H^3/E^{*2} of about 0.081 and 0.25, respectively. Further increasing the current of additional anode to 40 A, the properties would deteriorate due to the precipitation of *w*-AlN (wurtzite structure) induced by ion irradiation effect.

1. Introduction

High performance dry machining is one of the major trends in modern manufacturing. The dry cutting generates severe shear stresses and high temperature near the cutting zone, which consequently leads to a premature degradation of the tool. PVD tool-coaters and cutting tools costumers are seeking innovative solutions which could improve the performance and lifetime of tools [1]. Compared with traditional binary nitrides films (TiN and CrN), the TiAlN-based films have been well acknowledged for industrial applications due to the favorable combination of high hardness as well as oxidation resistance. However, there are two limiting factors of TiAlN-based films: (i) significant hardness reduction at higher temperatures [2], and (ii) relatively high friction-coefficient at high temperature [3]. Further improvement of surface properties was achieved by the doping of various elements, e.g. Cr [4], Si [5], or Zr [6] in compounds. Specially the Cr addition to TiAlN may restrain the spinodal decomposition by slowing the diffusion [7] and retard the growth kinetics of oxide scale [8]. The quaternary Ti-Al-Cr-N film can exhibit a substantial improvement of synthesized properties compared to the ternary TiAlN film [9].

The Ti-Al-Cr-N films can be fabricated by different physical vapor deposition (PVD) techniques. Among them, the cathodic arc deposition (CAD) process is well known for high ionization degree and better adhesion strength between the films and substrate [10]. However the higher ionization degree (perhaps > 80% [11,12]) refers to the ionization degree of metal atoms. On the contrary, the ionization degree of reactive gaseous still remains at a relatively low degree, particularly at sites far away from the vacuum arc sources. In general, a higher ionization degree and plasma density would lead to a denser structure and more optimized film quality. Some approaches have been developed to improve the plasma density with the help of external devices, including anode layer source [13,14], hot filament [15], hollow cathode [16], Kaufman-type ion gun [17], helicon-wave excited plasma sources [18]. A.M.A. Elrahman [19] utilized the PEMS method to improve the plasma density and a relatively lower density of micro-defects was detected on coatings. Veerasamy et al. [20] also demonstrated the better structure of ta-C:H films enhanced by linear ion source. They still have some shortcomings although a positive effect has been demonstrated. The anode layer source sometime leads to the atomic lattice distortion due to injection effect of energetic ions. The hot filament may suffer from the easy damage and the discharge instability due to surface oxides or carbides. An electrically enhanced discharge may be produced in the vacuum arc system to improve the plasma density. An electron collector e.g. the additional anode, is introduced and a DC power supply is
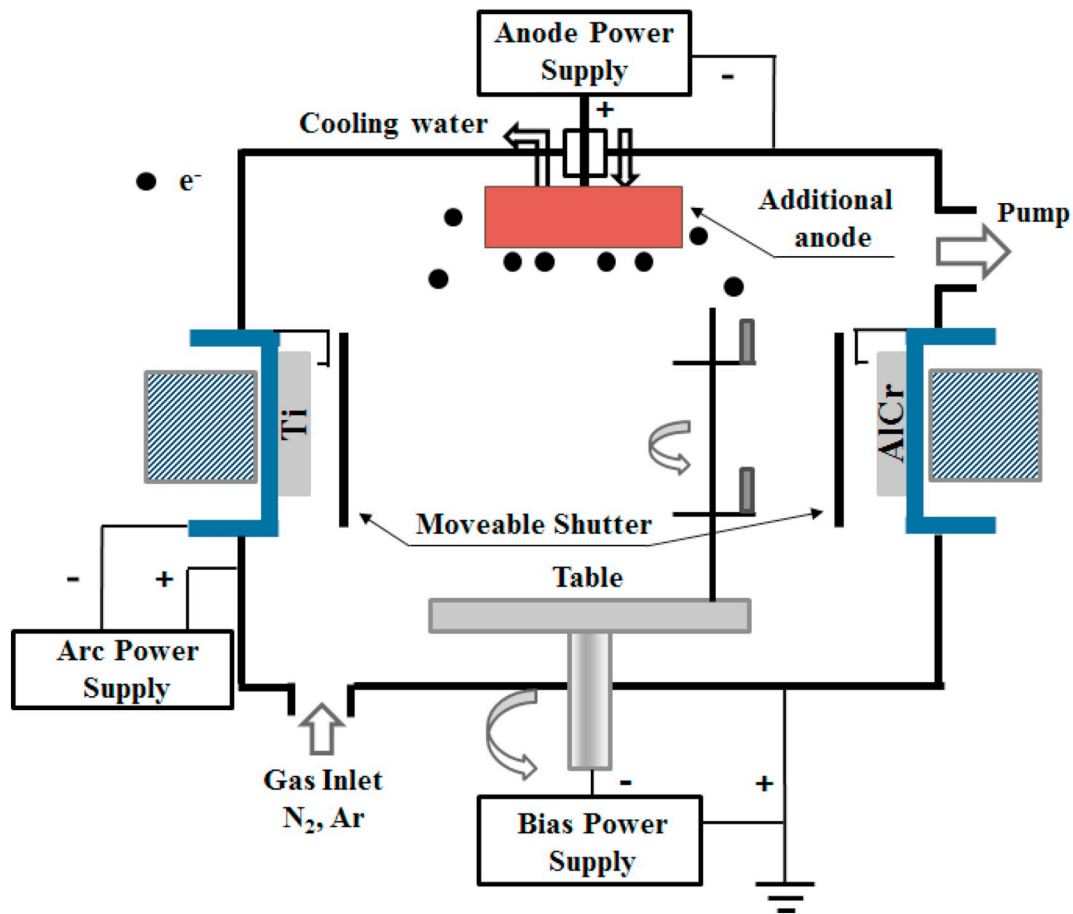
Fig. 1. Schematic diagram of the cathodic arc system with additional anode.

Table 1
Deposition parameters for Ti-Al-Cr-N films.

	Ti	TiN	Ti-Al-Cr-N films			
Base pressure (Pa)	3×10^{-3}					
Temperature (°C)	400					
Plasma etching	Ar plasma for 45 min at 1.5 Pa under substrate bias -200 V					
Current of additional anode (A)			0	20	30	40
Voltage of additional anode (V)			0	19.2	22.1	27.9
Bias voltage (V)	120	120	30			
Arc current (A)	100 (Ti target)	100 (Ti target)	100/100 (Ti and AlCr targets)			
N_2 flow rate (sccm)		155	500			
Deposition time (min)	15	25	120			

applied between the additional anode and the chamber wall. J.A. Sue, et al. [21] has utilized this enhanced discharge method in the sputtering stage of deposition processes, resulting in a sufficient adherence between film and substrate.

As utilized in sputtering cleaning stage, the enhanced discharge may have a positive effect. However, the application of additional anode in deposition of Ti-Al-Cr-N films has not been demonstrated before. In this paper, the evolution of the film structure and mechanical properties derived from the enhanced discharge is reported.

2. Experimental details

The Ti-Al-Cr-N films were deposited on polished Si (100) and M2 high speed steel (wt% , C-0.8%; Mn-0.3%; V-2%; Mo-5%; Si-0.45%; Cr-4%; Ni- < 0.3%; W-6% and Fe- balance.) in vacuum arc system. The schematic diagram of the system is shown in Fig. 1. The additional anode is a rectangular metal plate with the size of

905 mm × 100 mm × 25 mm, which is made of 304 stainless steel. The anode plate and vacuum chamber are connected to the anode and cathode of DC power supply respectively. The current of additional anode can be adjusted in range from 0 A to 100 A. The pure Ti (99.95%) and AlCr (99.95%) were used as arc targets. The substrates (Si stripes and M2 high speed steel (Φ20 mm × 4 mm)) were ultrasonically cleaned in ethanol. After rinsing in distilled water and drying in hot air, the substrates were placed on a two-fold rotating carousel, which kept the rotation speed of 15 rpm. The chamber was evacuated to below 3×10^{-3} Pa and the pressure was adjusted to 1.5 Pa by bleeding high-purity (99.999%) argon. The substrates were cleaned with argon plasma by arc-enhanced glow discharge at the pulsed bias of -200 V for 45 min in order to remove the native oxide layers from the substrates. The Ti and TiN interlayer are deposited respectively for 15 min and 25 min to improve the adhesion. Then the Ti and AlCr targets were evaporated at the arc current of 100 A and gas pressure of 3 Pa for 120 min. During the deposition, the biased voltage of -30 V, pulsed
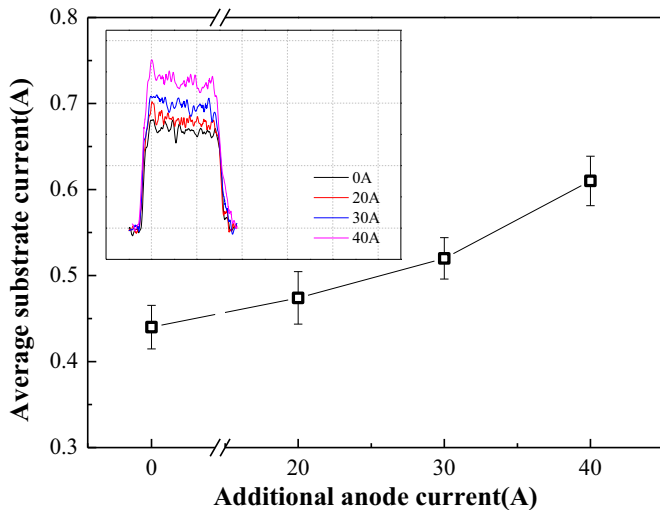
Fig. 2. Waveforms of pulsed substrate ion current and average substrate ion currents (I_{sub}) at different currents of additional anode.

frequency of 40 kHz, and duty cycle of 75% were utilized. The Ti-Al-Cr-N films were deposited with the current of additional anode of 0 A, 20 A, 30 A and 40 A, respectively. The detailed deposition parameters are listed in Table 1.

The substrate ion current was measured using a Tektronix digital oscilloscope via current sensor for the whole table assembly including the samples and holder. The plasma emission spectra in front of the Ti and AlCr cathodes were recorded using an optic spectrometer AvaSpec-2048FT-4-DT (Avantes, Holland), which was connected with the quartz fiber. The optical fiber aiming at the center of the Ti and AlCr cathode targets was used for light collection. The obtained emission signal ranged from 300 to 850 nm. The background spectral lines were eliminated automatically in all recorded spectra. The optical spectra were obtained by integrating the optical signal for 100 ms and 10 scans were averaged. The averaging steps eliminated the influence of spot motion. The optical emission intensities were measured during the whole period of the arc discharge. The spectral resolution is < 0.1 nm.

The structural analysis of films was performed by the grazing-incidence X-ray diffraction with Cu Kα radiation using a Bruker D8 diffractometer in Bragg/Brentano mode at 40 mA and 40 kV. The X-Ray was incident at a gracing angle of 2°, and scanning angular (2θ) was ranged from 20 to 90° at a scanning speed of 4°/min. The degree of preferred orientation for the Ti-Al-Cr-N films was determined by calculating the texture coefficient of the $(h\,k\,l)$ plane, T_{hkl}, defined as Eq. (1) [22]:

$$T_c(hkl) = \frac{I_m(hkl)_i / I_0(hkl)_i}{\left(\frac{1}{n}\right) * \sum_1^i I_m(hkl)_i / I_0(hkl)_i} \tag{1}$$

where I_m $(h\,k\,l)$ is the measured relative intensity of the reflection from the $(h\,k\,l)$ plane, I_0 $(h\,k\,l)$ is the relative intensity from the same plane in a standard reference sample, and n is the total number of the reflection peaks from the film. The value of the texture coefficient for the peaks under investigation ranges from unity for a randomly oriented sample, to n for a sample having a complete preferential orientation [23]. The surface micrographs, cross-section morphologies and the thickness of films were carried out by scanning electron microscope of Netherlands, FEI Quanta 200F. Residual stress of the coatings was calculated based on the $\cos^2\Psi\sin^2\Psi$ method, where Ψ is the angle between the normal to the coating surface and the diffracting lattice planes. The X-ray diffraction peak position shifts with the Ψ angle. The formula to calculate

the residual stress is [24]:

$$(d_{hkl} - d_0)d_0 = \frac{1}{2}S_2 * \sigma * \cos^2\alpha * \sin^2\Psi + \frac{1}{2}S_2 * \sigma * \sin^2\alpha + 2S_1 * \alpha \tag{2}$$

here, S_2 and S_1 are coating constants related to the Poisson's ratio and elastic modulus (determined by nanoindentation, different for the coatings with different thickness). α is the angle related to the 2θ diffraction angle and $\Psi = 0°$, 15°, 20°, 25°, 30°, 35°, 40° and 45°.

The hardness test was performed by the Fischerscope HM2000 nanoindenter equipped with a Berkovich indenter and computer-controlled measurement system. The software WIN-HCU was employed to determine the micro-hardness and elastic modulus. The measurements were conducted at constant indentation, whose depth was close to that 1/10th of the film thickness avoiding the effect of the relatively soft substrate. Five different positions were performed to improve accuracy. The adhesion of the Ti-Al-Cr-N films was evaluated by Rockwell indentation test using a Rockwell C diamond stylus (cone apex angle 120° and tip radius R of 0.2 mm) at an applied load of 150 kg.

3. Results and discussion

3.1. Substrate ion current and optical emission spectra

The waveforms of pulsed substrate current and average substrate current (I_{sub}) measured in nitrogen atmosphere ($P_{N2} = 3$ Pa) are depicted in Fig. 2. The substrate current increases gradually with the increase of the current of additional anode (the voltage of additional anode also increases, Table 1). The I_{sub} is composed of both ions and secondary electrons from the substrate surface, which may reflect the plasma density near the substrate in the system. The I_{sub} increased by 39.6% at the additional anode current of 40A than that without the discharge of additional anode. This indicates a higher ionization degree in the deposition system and an enhanced plasma density around samples [25].

Fig. 3 presents the optical emission spectrum (OES) of nitrogen, titanium, chromium and aluminum at different currents of additional anode. The changes of peak position and the categories of particles are very slight and the relative magnitudes of OES intensity are altered once the current of additional anode appears. The higher emission lines of nitrogen active particles (Fig. 3(e, f)) indicate that the additional anode enhances the discharge and causes an increase in plasma density and electron temperature [26]. However, it should be pointed out that the increase in the emission spectrum intensity of titanium, chromium and aluminum (Fig. 3(a, b and c, d)) is very slight, compared to the tremendous increase in the emission spectrum intensity of nitrogen active particles. It suggests that the additional anode produces a more effect on the nitrogen gas than evaporated target materials.

Fig. 4 depicts the variation of representative N* (758.7 nm), N$^+$ (654.4 nm), N^{2+} (650.5 nm), Ti$^+$ (323.9 nm), Ti^{2+} (337.2 nm), Cr$^+$ (356.3 nm), Cr^{2+} (315.8 nm), Al$^+$ (396.2 nm) and Al^{2+} (452.9 nm) emission intensities versus the current of additional anode. The spectral intensity of N* (758.7 nm), N$^+$ (654.4 nm) and N^{2+} (650.5 nm) at the current of additional anode of 40A is increased by 157.8%, 157.1% and 149.5% respectively compared to that without the current of additional anode. In order to roughly characterize the amount of the ionized nitrogen, the sum (C_{um}) of C_{N*}, C_N^+ and C_N^{2+} is calculated to demonstrate the relative increase of the ionized nitrogen (where the C_{N*}, C_N^+ and C_N^{2+} mean the intensity of excited nitrogen, the intensity of N$^+$ and the intensity of N^{2+}, respectively). Compared with the usual arc discharge, the C_{sum} is increased by 28%, 62% and 155% with the anode current of 20 A, 30 A and 40 A respectively. In contrast, the spectral intensity of Ti$^+$ (337.2 nm) and Ti^{2+} (323.9 nm) at additional anode current of 40 A only increase by 14.6% and 9.3%, respectively. Also, the
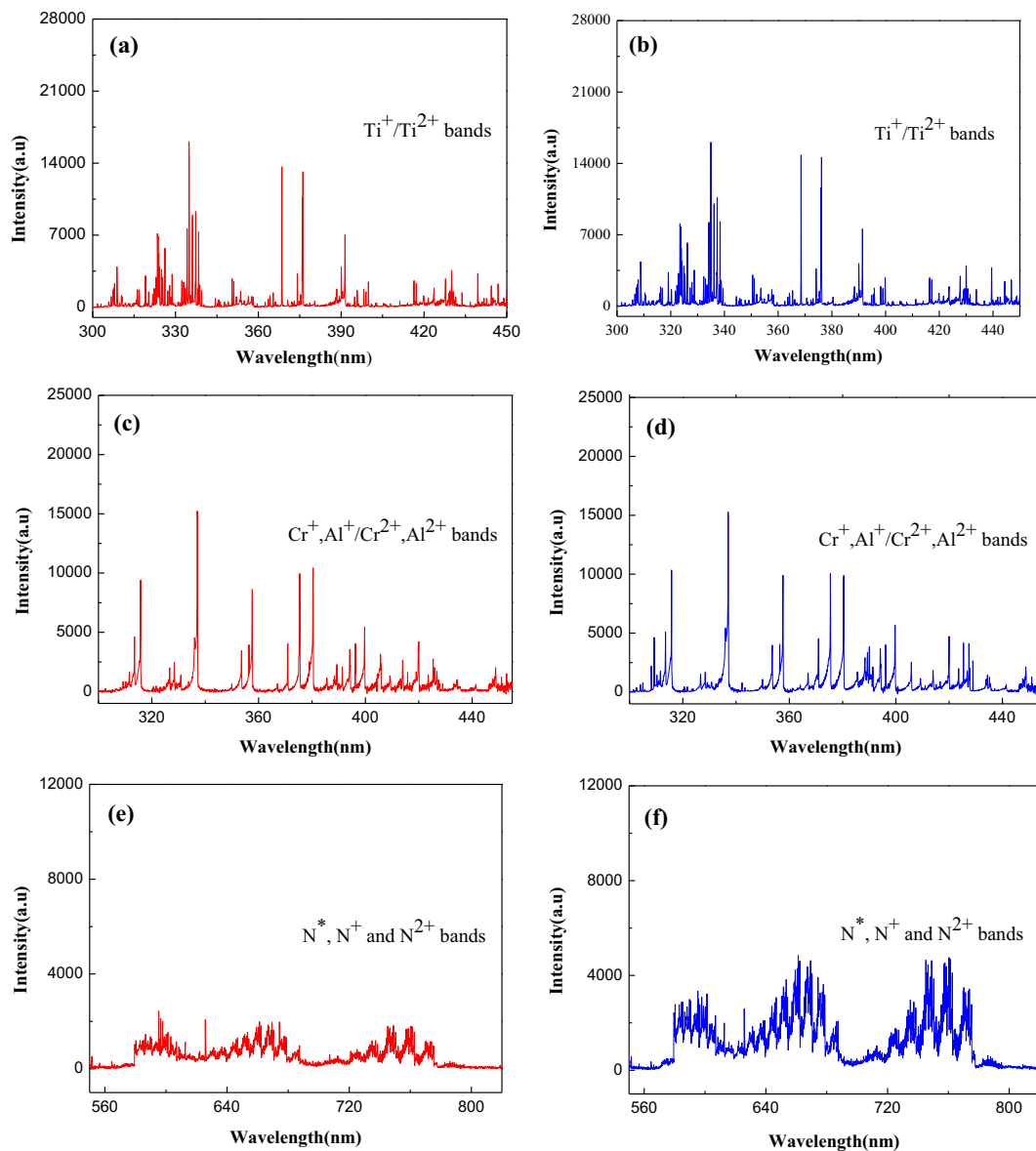
Fig. 3. Optical emission spectrum intensity of different species: (a) Ti^+ and Ti^{2+}, 0 A, (b) Ti^+ and Ti^{2+}, 40 A, (c) Cr^+, Al^+, Cr^{2+} and Al^{2+}, 0 A, (d) Cr^+, Al^+, Cr^{2+} and Al^{2+}, 40 A, (e) N^*, N^+ and N^{2+}, 0 A, (f) N^*, N^+ and N^{2+}, 40 A.

spectral intensity of Cr^+ (356.3 nm), Cr^{2+} (315.8 nm), Al^+ (396.2 nm) and Al^{2+} (452.9 nm) emitted from the AlCr cathode remains nearly unchanged with increasing the current of additional anode (Fig. 4(c)).

The excitation and ionization of the nitrogen occurs to a large extent as a result of collisions between electrons [27]. The excitation process can be described by Eqs. (3) and (4) [28].

$$N_2 + e^- \rightarrow N^* + N^* + e^- \tag{3}$$

$$N_2 + e^- \rightarrow N_2^+ + e^- \tag{4}$$

When the current of additional anode is 0 A, the electrons emitted from cathode target preferred to transfer towards the chamber wall nearby. The excitation of neutral nitrogen molecules induced by electronic collision is constrained to a relatively low degree. When a DC power supply is connected to between additional anode and vacuum chamber, the distribution of electric field in the vacuum chamber would be changed. And the plasma potential may also be more positive [29]. The electric potential of additional anode is much higher than that of

the arc cathode target as well as chamber wall (Table 1), consequently most of electrons fly towards the additional anode in spite of a long pathway. The utilization efficiency of electrons is enhanced, which could contribute to more collision. This leads to more excitation of nitrogen. Higher spectral intensity of N^*, N^+ and N^{2+} was achieved, suggesting that the number of active nitrogen particles was increased effectively in the deposition system. A higher plasma density may be achieved with a higher ion flux towards the substrate surface. In contrast, the spectral intensity of metal ions hardly changes regardless of anode current.

The energy delivered to the growing film has also a crucial effect on its structure, phase composition and physical properties. E_{bi} is defined as conversion of the energy of bombarding ions and it can be expressed by the following formula [30]:

$$E_{bi} = (U_s I_A t_d)/S_A D \tag{5}$$

(where the U_s, I_A, t_d, S_A and D are negative bias, substrate current, deposition time, substrate area and the film thickness, respectively). In
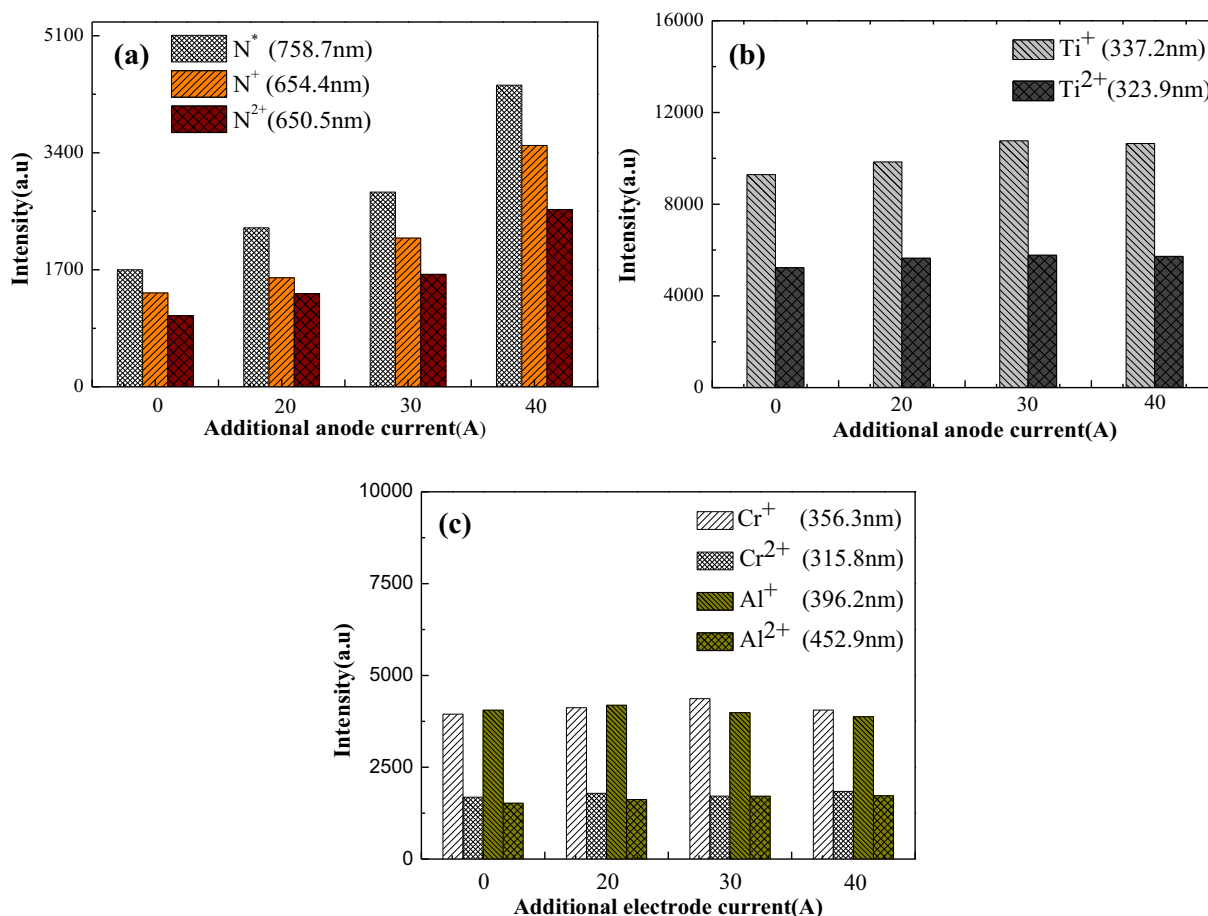
Fig. 4. OES intensity of representative species: (a) N^*, N^+ and N^{2+}, (b) Ti^+ and Ti^{2+}, (c) Cr^+, Cr^{2+}, Al^+ and Al^{2+}.

our experiments, the U_s, t_d and S_A are constant, and the E_{bi} value is determined by the ratio of substrate ion current and thickness of films. The substrate current is proportional to the number of incident ions to the sample. The higher ion flux (Fig. 2) implies a larger E_{bi} value, which would be beneficial for the achievement of the denser films [31].

3.2. Microstructure of Ti-Al-Cr-N films

Fig. 5 shows the surface morphology of the Ti-Al-Cr-N films deposited at different currents of additional anode. Many macro-particles (MPs) with various sizes, resulting from the droplets emitted from the arc spots on the targets, are observed on the surfaces of films, which are frequently encountered in cathodic arc deposition process. The Image-Pro Plus software is employed in order to precisely investigate the density of MPs and distribution fractions of MPs sizes on the film surface (as presented in Table 2).

Without the discharge of additional anode, the number density of unit area and size of MPs are the largest. They decrease distinctly with increasing the current of additional anode from 0A to 30A. The film deposited at the current of 30A possesses the smallest number density of MPs ($0.84 \times 10^6 \, \text{mm}^{-2}$). Several reasons might be accounted for it: 1) with higher plasma density, the macroparticles are more charged by electrons [32] and the negatively charged macroparticles would be repelled away from the substrate when the pulsed negative bias was exerted, 2) the combination effect of higher residual stress (-4.3GPa) and increased atom mobility may result in a reduction of the density of MPs [33,34] with increasing anode current, 3) much more ion bombardment also lead to the removal of some macroparticles. Thereby, the

surface of deposited films becomes smoother with additional discharge. Further increasing the current of additional anode to 40A, the number-density of MPs slightly increases again. The amount of ionized nitrogen is sharply increased in vacuum chamber. The bombardment energy of ions would convert into surface heat, which made the macroparticles more adherent on the surface and caused an increase of number-density of MPs eventually [35]. Besides, the discharge of additional anode occurs between the utilized anode and the chamber wall at the negative potential. The ions near the wall may bombard intensively the wall surface and some contaminations may be excited and sputtered away. It will also contribute to the increase of MPs on the sample surface. Therefore, a proper current of additional anode is utilized to increase plasma density but not to produce more contaminations.

Fig. 6 illustrates the cross-sectional micrographs of Ti-Al-Cr-N films. In spite of the dense columnar microstructure, more fracture facets are observed for these samples with the current of additional anode, indicating the deflection of micro-cracks. It means larger fracture-resistance. Fig. 7 summaries the change of the film thickness (D) and E_{bi} value at different currents of additional anode. The film thickness (D) increases slightly when the current of additional anode goes up from 0 to 20 A. However a further increase of the current of additional anode leads to the decrease of film thickness. The introduction of the additional electric field can result in a higher ionization degree of reactive gas, and more ionized flux towards substrates. This may be beneficial for the denser structure of deposited films. If the additional discharge is more intensive, the excessively ionized flux may bombard the substrate leading to the re-sputtering effect, which is responsible for the decreased thickness. As shown in Fig. 7, the E_{bi} value increases with the
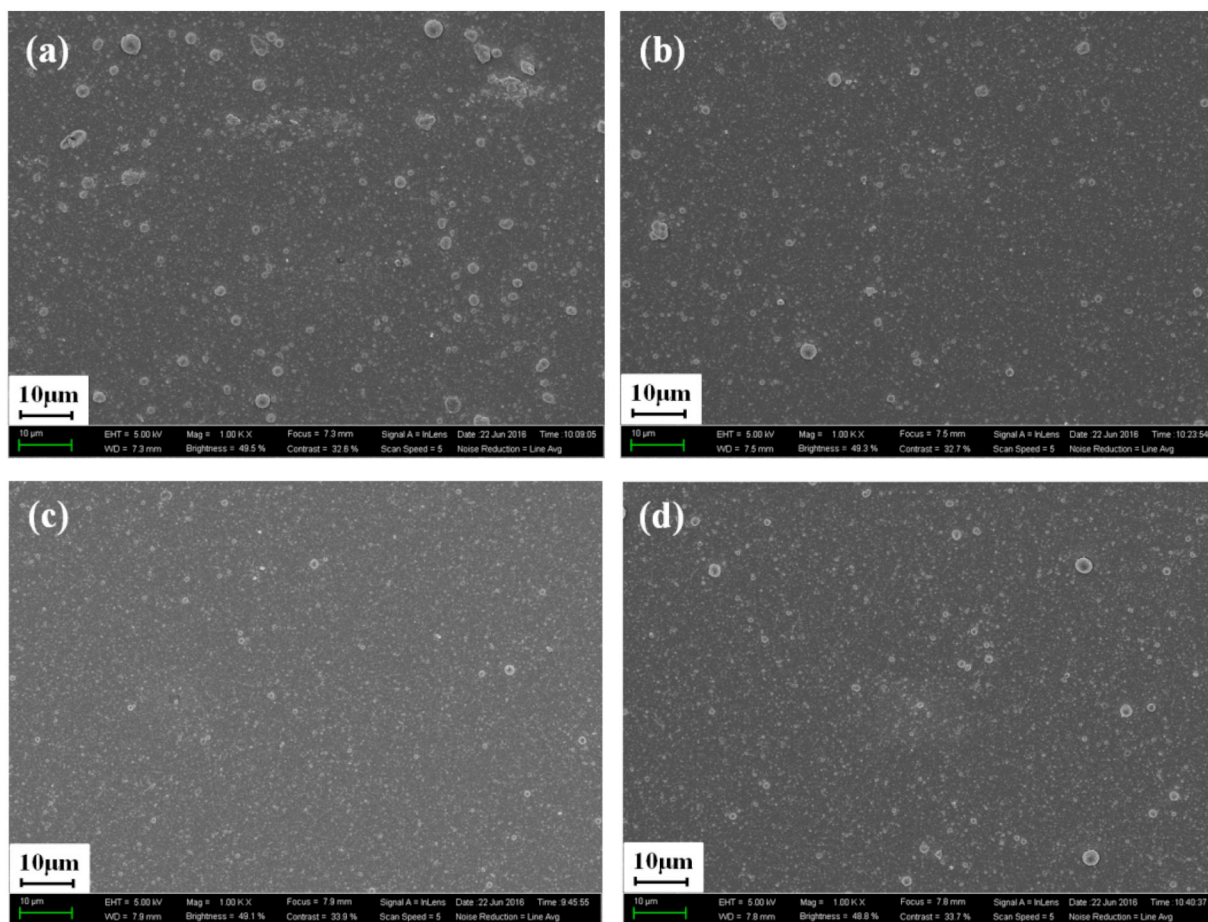
Fig. 5. Surface micrograph of Ti-Al-Cr-N films deposited at different currents of additional anode: (a) 0 A (b) 20 A (c) 30 A (d) 40 A.

Table 2
The compositions of the samples, the MPs density on the films' surface and dimensional fractions.

Additional anode current(A)	Compositions				MPs densities per $mm^{-2} \times 10^6$	Distribution [%]		
	Ti	Al	Cr	N		0–0.35 μm	0.35–0.75 μm	0.75–1.25 μm
0A	39.5	23.3	16.5	20.7	2.14	46	41	13
20A	32.4	27.1	20.4	20.1	1.67	58	34	8
30A	30.7	28.8	21.1	19.4	0.84	80	19	1
40A	29.6	29.5	20.8	20.1	1.32	72	22	6

increase of the current of additional anode. It may be helpful for the surface properties to some extent.

Fig. 8 illustrates the diffractograms for the Ti-Al-Cr-N films deposited at different currents of additional anode. As expected, the crystalline microstructure matches with the NaCl-B1 type structure (FCC) of titanium aluminum chromium nitride and aluminum nitride (JCPDS card # 01-070-2942 [36] and 03-065-3762 [37]). Additionally, the diffraction peaks of Si (100) are also visible (the (100)-oriented Si stripes were acted as substrates). The Ti-Al-Cr-N film deposited at the current of additional anode of 0A presents (111), (200) and (002) peaks. With the current of additional anode of 30A, the diffraction intensity of the (200) peak increases accompanied with a disappearance of the (002) peak and a decreased intensity of (111) peak. When the current of additional anode further increases to 40A, the diffraction intensity of (111) peak and (200) peak exhibits different changes. The wurtzite phase ((002)) appears again.

Based on the measured reflection intensities, the two major (111)

and (200) XRD reflexes are focused (T_{111} and T_{200}, where T_{111} and T_{200} are the texture coefficient of the plane of (111) and (200)) to determine the preferred crystal lattice orientations of the films. The influence of the current of additional anode on the T_{111} and T_{200} of the Ti-Al-Cr-N films is shown in Fig. 9. Generally speaking, the preferred orientation of films is caused by the driving force to lower the overall energy of the film which is composed of the surface energy and strain energy [38,39]. At lower anode current (e.g., < 20 A), the Ti-Al-Cr-N films exhibit the preferred orientation of (111) with the lowest strain energy when the strain energy is dominant. With increasing the current of additional anode to 30A, the higher liquidity and diffusion migration ability of particles would decrease the surface energy of films. Consequently, the Ti-Al-Cr-N film would grow towards the orientation of a mixed (111) and (200) plane in order to minimize the total energy. At the current of additional anode of 40A, the film texture changes to a (111) preferred orientation again. The excessive bombarding ions would knock surface atoms deeper into the subsurface of the growing films and get
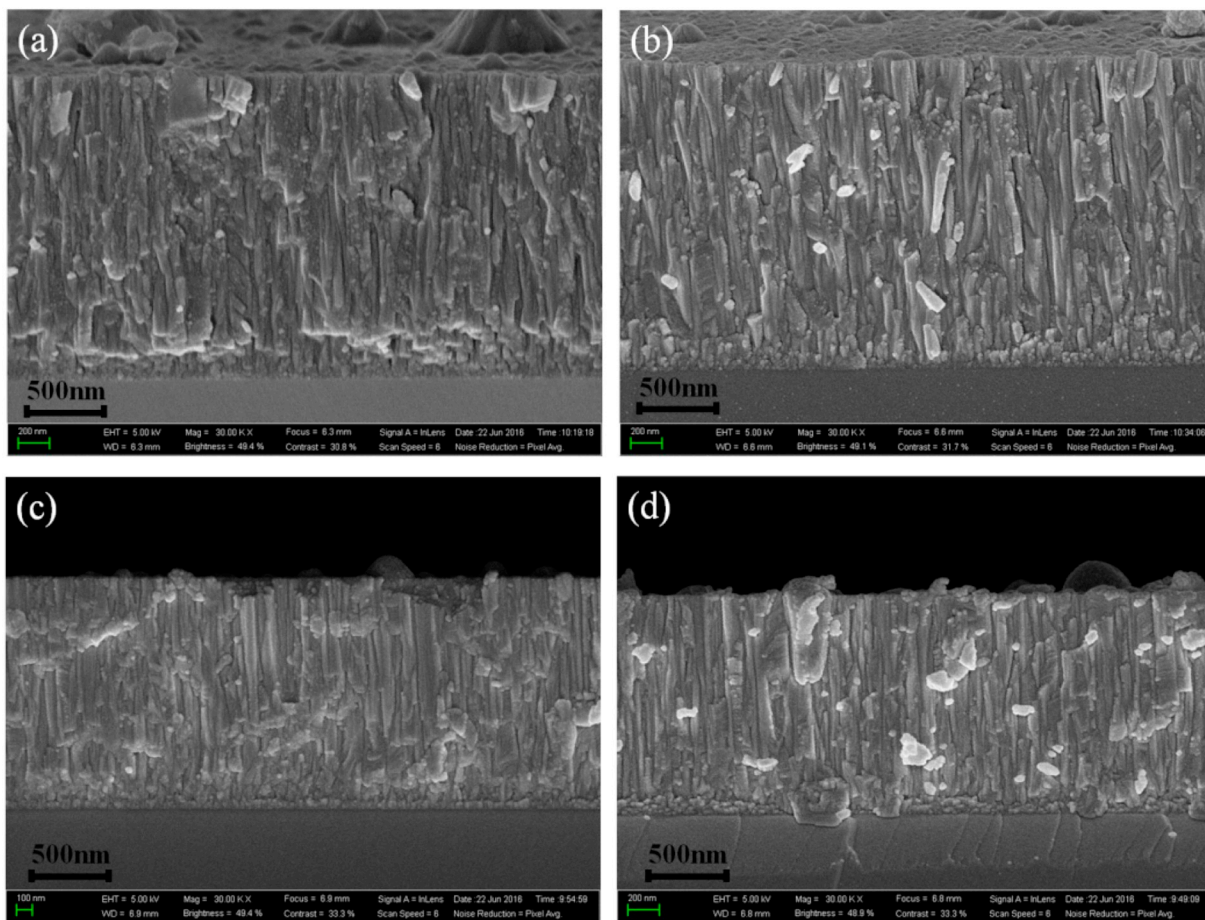
Fig. 6. Cross-sectional micrographs of the Ti-Al-Cr-N films deposited at different currents of additional anode: (a) 0 A (b) 20 A (c) 30 A (d) 40 A.
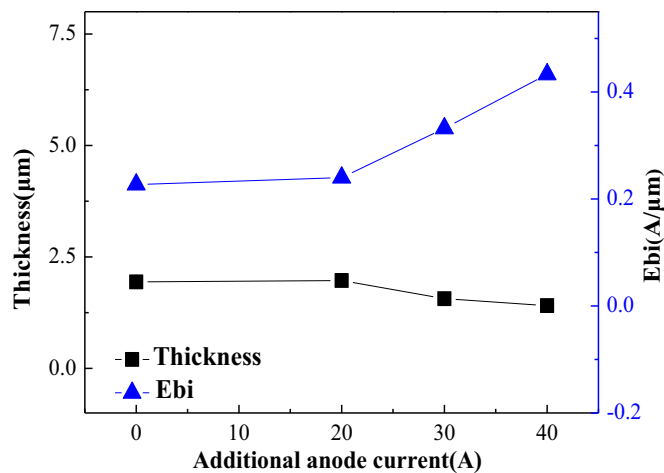

Fig. 7. Thickness and E_{bi} value of Ti-Al-Cr-N film at different currents of additional anode.

Fig. 8. X-ray diffraction patterns of the Ti-Al-Cr-N films as a function of current of additional anode: (a) 0 A (b) 20 A (c) 30 A (d) 40 A.

themselves trapped in the layer. The associated additional volume in the constrained layer leads to an expansion of the film and the entrapped atoms elevate strain energy.

According to the XRD patterns, the grain size can be calculated by the Scherrer's formula [40]. This method is based on a relatively rough estimation of the crystallite size, since the fitting method used to determine the full width at half maximum of the diffraction peaks cannot
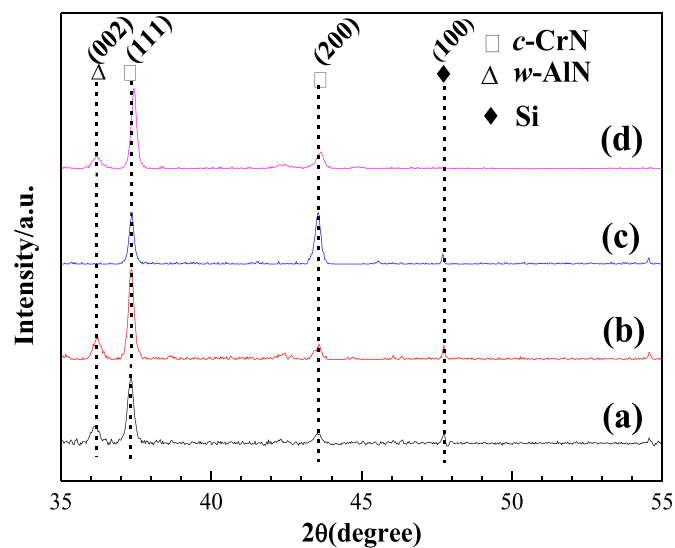
take precisely into account the shape of crystallite size distribution. Fig. 10(a) demonstrates the change of grain size of Ti-Al-Cr-N films at different currents of additional anode. With increasing the current of additional anode from 0A to 30A, a slight broadening of the (200) peak
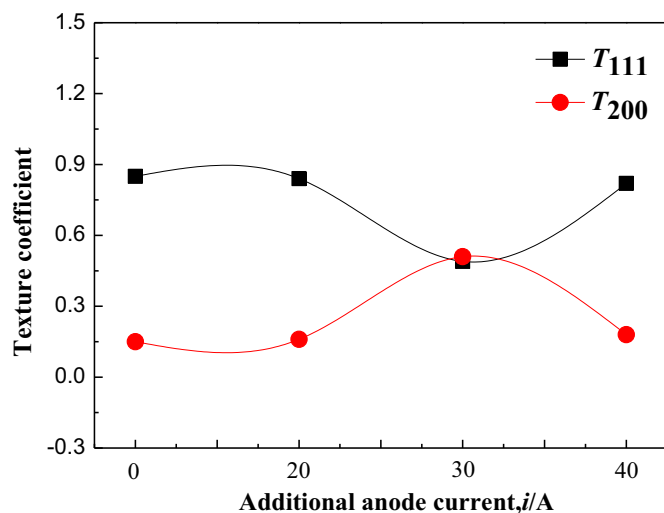
Fig. 9. Influence of the current of additional anode on the T_{111} and T_{200} of the Ti-Al-Cr-N films.

is observed. The grain size (for the (200) plane) decreases from 17.4 nm to 13.9 nm. A higher flux of incident ions could result in more defects generated in the surface thereby increasing the number of preferential nucleation sites and thus decreasing the grain size [41]. Further increasing the anode current to 40 A, the grain size increased slightly to 14.5 nm, which is related to increased migration of grain boundaries resulting from excessive ion bombardment (40 A) [42].

Fig. 10(b) demonstrates the residual stress and lattice parameter variation as a function of the current of additional anode. The residual stresses are measured using the $\cos^2\Psi\sin^2\Psi$ method and the lattice parameter is evaluated from Nelson-Riley function [43]. The internal stress increases from -2.7 GPa to -5.8 GPa with increasing the current of additional anode from 0 A to 40 A, which is attributed to the effect of atomic peening. This is in relatively good agreement with previous findings reported by J. Lin [44]. Excessive ion bombardment induces the accumulation of the residual stress and exerts an effect on the mechanical properties of films. The lattice parameter decreases with increasing the current of additional anode. It may be attributed to more incorporation of Al atoms in the films (as presented in Table 2), which leads to contraction of the lattice [45].

Fig. 11 exhibits the illustration of film-growth process with/without additional anode. During the usual arc discharge (without additional anode), the electrons derived from cathode target would flow to chamber wall under the electric field. In the flight path, the electrons would collide with neutral and/or excited gas molecules and cause the ionization of gas. The introduction of additional anode would change

the flight trajectory of electrons and enhance the collision probability. The additional anode is located far away from the cathodic arc source and the potential is higher than the chamber wall. Therefore the discharge is enhanced and a higher ion flux flies towards the substrate. The high ion flux could promote atoms/ions to move or diffuse into the inter-grain voids, break down the growth of large columnar grains, and create more nucleation sites. The closer-packed arrangement of particles would directly lead to the densification of films and further influence the surface properties of films [46].

3.3. Mechanical properties of Ti-Al-Cr-N films

Fig. 12(a) depicts the hardness and elastic modules of Ti-Al-Cr-N films as a function of current of additional anode. Each value is the averaged result of ten indents, and the error bars are determined from the standard deviation of those indents. Without the discharge of additional anode, the hardness and elastic modulus of Ti-Al-Cr-N film are around 25.1 GPa and 300.3 GPa, respectively. They increase to 26.7 GPa and 307.4 GPa, respectively, with the current of additional anode of 20A. The maximum hardness (31.3 GPa) and elastic modulus (342.5 GPa) are achieved with the current of additional anode of 30A. Several factors would contribute to the enhancement of surface hardness. Higher stress (-4.3 GPa) plays an important role [47]. Owing to the intensive ion peening, the penetration into the lattice of the condensed films and generation of defects are promoted. These defects would induce the pinning effect and act as an obstacle for movement of the dislocations, which may improve the hardness [48]. The improved densification of film inferred from the higher E_{bi} value (0.332) also plays a positive role in the hardness. Besides, the growth of deposited film (30A) demonstrates the preferred (200) and (111) plane. The strengthening mechanism may also be related to the effect of the texture [49]. A much larger current of additional anode (e.g., 40 A) decreases the hardness of the film. The intensive ion bombardment effect would act an impact on the surface mobility of the deposited species and their intermixing, and induce the precipitation of the wurtzite phase. The formation of w-AlN phase would decrease the hardness of films [50]. Alternatively, the cubic structure of film changed to a (c, w)-mixture structure (40 A). The relaxation of lattice caused by the superfluous bombarding energies could lead to a decreased hardness of deposited film [51].

The H/E* and H³/E*² may be calculated from the hardness (H) and effective elastic modulus (E*) of the film (where E* = E/(1-ν^2) is the effective Young's modulus and ν is the Poisson ratio, respectively). The H/E* is described as the deformation relative to yielding of the hard films and the H³/E*² value is an index of the resistance to plastic deformation [52] for films. The higher the ratio is, the higher the resistance of the film to plastic deformation. Fig. 12(b) shows the H/E* and H³/E*² value of Ti-Al-Cr-N film as a function of the current of
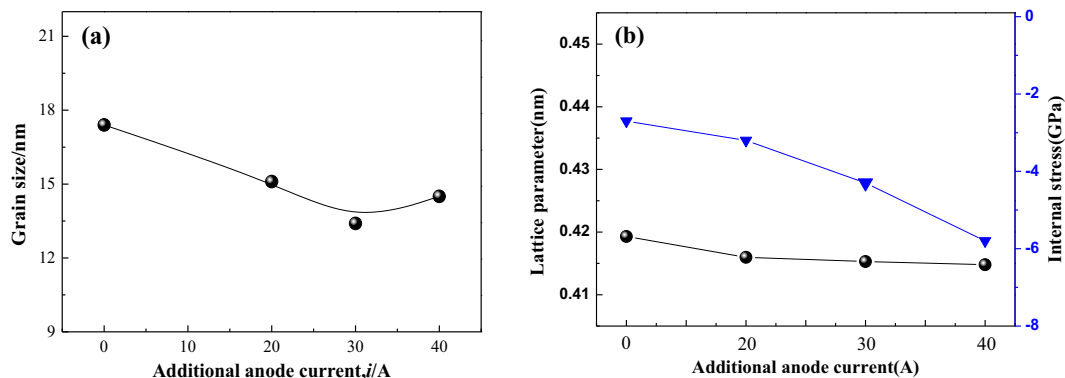

Fig. 10. Variation of grain size, lattice parameter and internal stress as a function of current of additional anode: (a) grain size, (b) lattice parameter and internal stress.
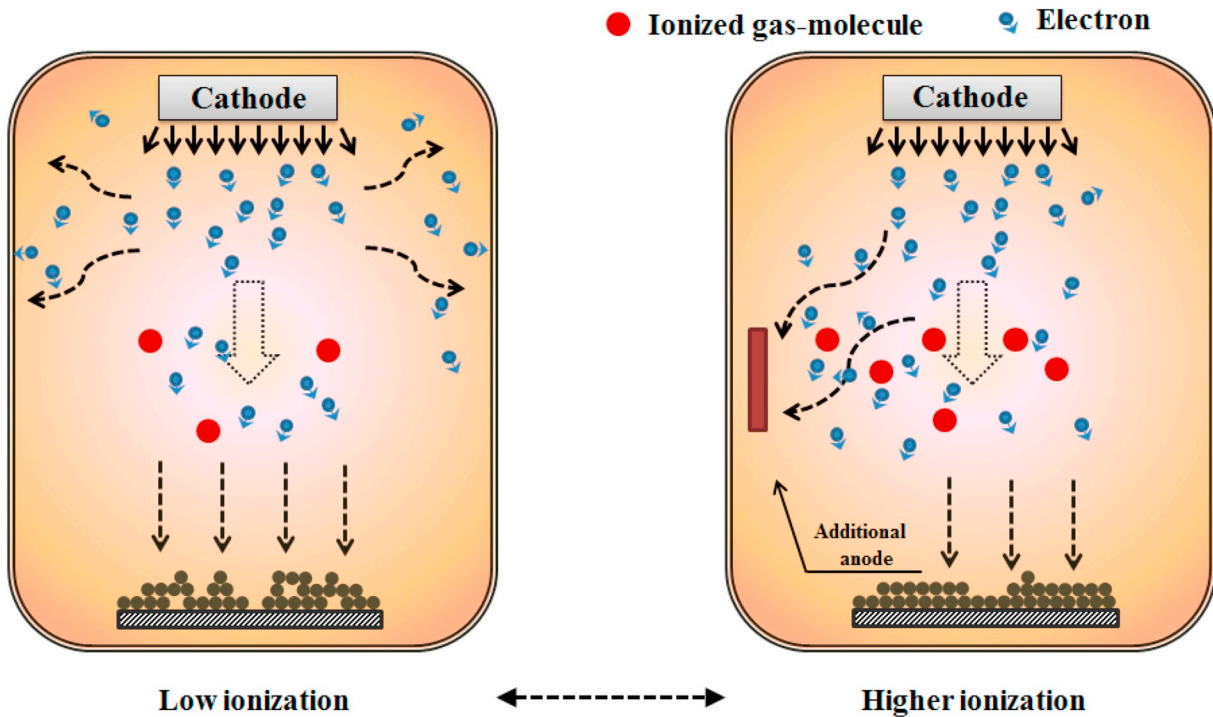
Fig. 11. Film-forming process of particles with/without additional anode.
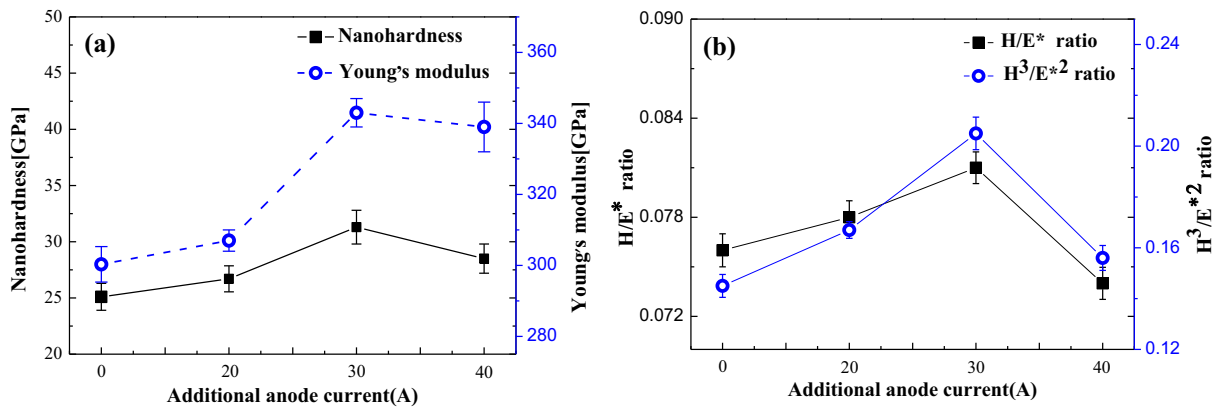

Fig. 12. Nanoindentation results of Ti-Al-Cr-N films as a function of current of additional anode: (a) Nanohardness (H) and Young's modulus (E), (b) H/E* and H^3/E^{*2} value.

additional anode. The discharge of additional anode leads to a higher H/E* and H^3/E^{*2}. The highest H/E* and H^3/E^{*2} ratio of about 0.081 and 0.25 GPa are produced with the current of additional anode of 30A. It infers an enhanced resistance of film to cracking and highly elastic recovery with fewer cracks in unloading stage with diamond indenter.

Fig. 13 presents the micrographs of indentations within a Daimler Benz Rockwell C adhesion test. In contrast with the indentation binding strength standard drawing VDI 3198 [53], all the Ti-Al-Cr-N films show an adequate adhesion strength value to the substrates. It is featured by no larger area of exposed substrate and insignificant delamination around the indents. The films prepared without the discharge of additional anode exhibits a slight peeling indicating the adhesion strength of HF3. With the discharge of additional anode, the adhesion strength between films and substrate is enhanced. The indentations are clear and smooth without cracks and dew point along the edge of indentation, which exhibits the best adhesion strength (HF1) at the current of additional anode of 30A. Energetic ion bombardment may lead to a

compact structure and small grain size, which prevents the extension of crack effectively [54]. With the current of additional anode of 40A, significant delamination along the indent boundary is observed (HF3). Larger ion bombardment may produce brittle interface [55]. Additionally, the poor adhesion may be correlated to the increased residual stress in the film.

4. Conclusion

The Ti-Al-Cr-N films have been fabricated using electrically enhanced arc discharge technology. The results show that the introduction of additional anode discharge has increased substantially the plasma density and substrate currents. It is attributed to the enhancement of nitrogen excitation/ionization induced by the stronger electric field intensity. With increasing the current of additional anode, the E_{bi} has been improved leading to compact structure and small grain size of the films. The Ti-Al-Cr-N film deposited at the current of additional
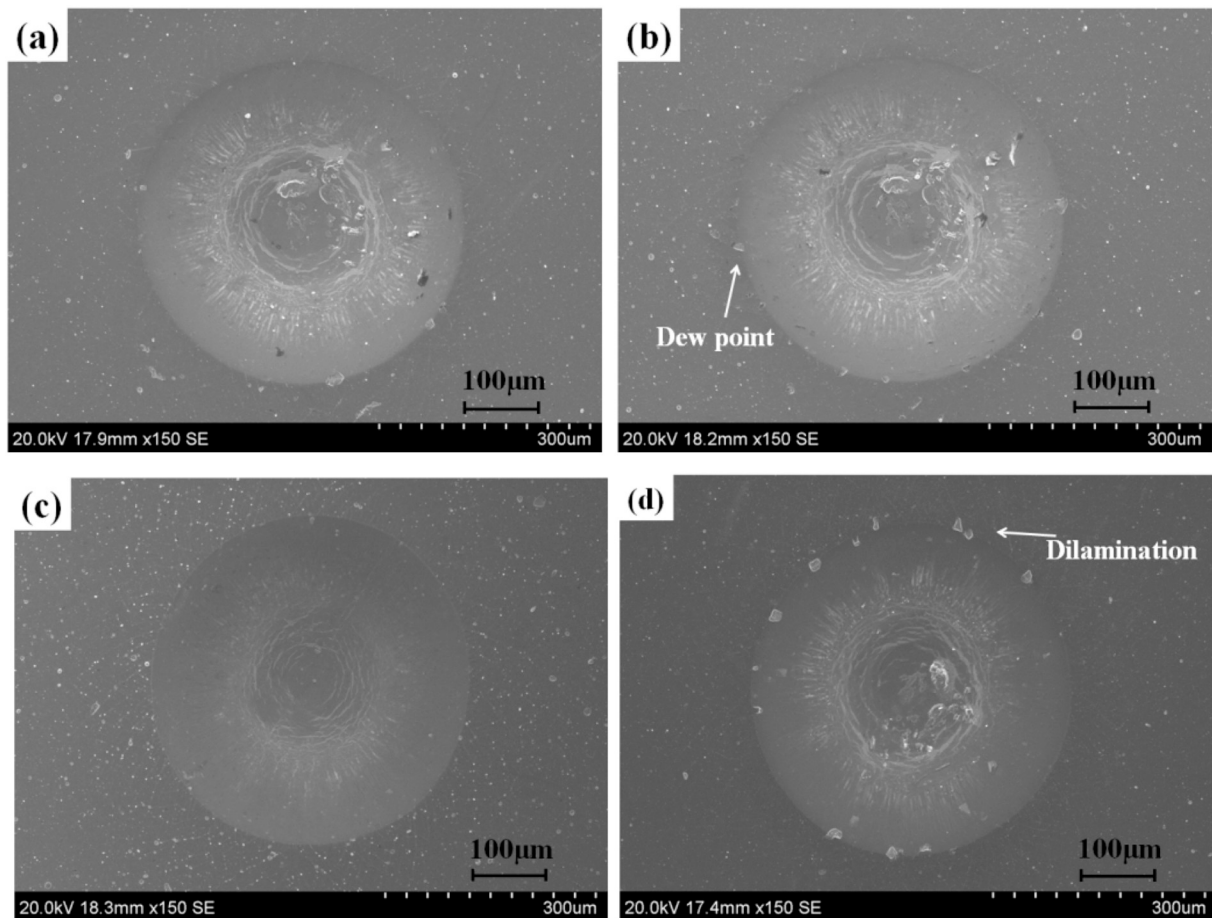
Fig. 13. Indentation morphology of Ti-Al-Cr-N films at different currents of additional anode: (a) 0A (b) 20 A (c) 30A (d) 40 A.

anode of 30A possesses the highest hardness and optimized adhesion strength between the film and substrate. A higher anode current (e.g., 40A) may weaken the surface properties of films due to the precipitation of *w*-Al phase and high internal stress induced by excessive bombardment of ions.

References

[1] Inspektor, P.A. Salvador, Architecture of PVD coatings for metal cutting applications: a review, Surf. Coat. Technol. 257 (2014) 138–153.

[2] W. Munz, Titanium aluminum nitride films: a new alternative to TiN coatings, J. Vac. Sci. Technol. A 4 (1986) 2717–2725.

[3] S.C. Veldhuis, G.K. Dosbaeva, K. Yamamoto, Tribological compatibility and improvement of machining productivity and surface integrity, Tribol. Int. 42 (2009) 1004–1010.

[4] Y.X. Xu, L. Chen, F. Pei, Y. Du, Structure and thermal properties of TiAlN/CrN multilayered coatings with various modulation ratios, Surf. Coat. Technol. 304 (2016) 512–518.

[5] L. Zhu, M. Hu, W. Ni, Y. Liu, High temperature oxidation behavior of $Ti_{0.5}Al_{0.5}N$ coating and $Ti_{0.5}Al_{0.4}Si_{0.1}N$ coating, Vacuum 86 (2012) 1795–1799.

[6] L. Chen, D. Holec, Y. Du, P.H. Mayrhofer, Influence of Zr on structure, mechanical and thermal properties of Ti-Al-N, Thin Solid Films 275 (2015) 5503–5510.

[7] M. Danek, F. Fernandes, A. Cavaleiro, T. Polcar, Influence of Cr additions on the structure and oxidation resistance of multilayered Ti-Al-Cr-N films, Surf. Coat. Technol. 313 (2017) 158–167.

[8] H.C. Barshilia, N. Selvakumar, B. Deepthi, K.S. Rajam, A comparative study of reactive direct current magnetron sputtered CrAlN and CrN coatings, Surf. Coat.

Technol. 201 (2006) 2193–2201.

[9] D.A. Delisle, J.E. Krzanowski, Surface morphology and texture of TiAlN/CrN multilayer coatings, Thin Solid Films 524 (2012) 100–106.

[10] J. Romeroa, M.A. Gómez, J. Esteve, F. Montalà, L. Carreras, M. Grifol, CrAlN coatings deposited by cathodic arc evaporation at different substrate bias, Thin Solid Films 515 (2006) 113–117.

[11] C. Yang, B. Jiang, Z. Liu, J. Hao, L. Feng, Structure and properties of Ti films deposited by dc magnetron sputtering, pulsed dc magnetron sputtering and cathodic arc evaporation, Surf. Coat. Technol. 304 (2016) 51–56.

[12] S. Paldey, S.C. Deevi, Single layer and multilayer wear resistant coatings of (Ti,Al) N: a review, Mater. Sci. Eng. A 342 (2003) 58–79.

[13] M. Kahn, M. Cekada, R. Berghauser, W. Waldhauser, C. Bauer, C. Mitterer, E. Brandstätter, Accurate Raman spectroscopy of diamond-like carbon films deposited by an anode layer source, Diam. Relat. Mater. 17 (2008) 1647–1651.

[14] M. Kahn, M. Čekada, T. Schöberl, R. Berghauser, C. Mitterer, C. Bauer, W. Waldhauser, E. Brandstätter, Structural and mechanical properties of diamond-like carbon films deposited by an anode layer source, Thin Solid Films 517 (2009) 6502–6507.

[15] R. Wei, E. Langa, C. Rincon, J.H. Arps, Deposition of thick nitrides and carbonitrides for sand erosion protection, Surf. Coat. Technol. 201 (2006) 4453–4459.

[16] D. Kim, Y. Han, J.S. Cho, S.K. Koh, Low temperature deposition of ITO thin films by ion beam sputtering, Thin Solid Films 377–378 (2000) 81–86.

[17] S. Nishizawa, T. Tsurumi, H. Hyodo, Y. Ishibashi, N. Ohashi, M. Yamane, O. Fukunaga, Structural changes in ZnO/NiO artificial superlattices made by ion beam sputtering, Thin Solid Films 302 (1997) 133–139.

[18] K. Yamaya, Y. Yamaki, H. Nakanishi, S. Chichibu, Use of a helicon-wave excited plasma for aluminum-doped ZnO thin-film sputtering, Appl. Phys. Lett. 72 (1998) 235–237.

[19] A.M.A. Elrahman, R. Wei, A comparative study of conventional magnetron sputter deposited and plasma enhanced magnetron sputter deposited Ti-Si-C-N nano-composite coatings, Surf. Coat. Technol. 241 (2014) 74–79.

[20] V.S. Veerasamy, H.A. Luten, R.H. Petrmichl, S.V. Thomsen, Diamond-like amorphous carbon coatings for large areas of glass, Thin Solid Films 442 (2003) 1–10.

[21] J.A. Sue, A.J. Perry, J. Vetter, Young's modulus and stress of CrN deposited by cathodic vacuum arc evaporation, Surf. Coat. Technol. 68 (1994) 126–130.

[22] M.I. Jones, I.R. Mccoll, D.M. Grant, Effect of substrate preparation and deposition conditions on the preferred orientation of TiN coatings deposited by RF reactive sputtering, Surf. Coat. Technol. 132 (2000) 143–151.

[23] Y.H. Cheng, B.K. Tay, Development of texture in TiN films deposited by filtered

cathodic vacuum arc, J. Cryst. Growth 252 (2003) 257–264.

[24] C.H. Ma, J.H. Huang, H. Chen, Residual stress measurement in textured thin film by grazing-incidence X-ray diffraction, Thin Solid Films 418 (2002) 73–78.

[25] K.D. Bouzakis, N. Michailidis, G. Skordaris, S. Kombogiannis, S. Hadjiyiannis, K. Efstathiou, E. Pavlidou, G. Erkens, S. Rambadt, I. Wirth, Optimisation of the cutting edge roundness and its manufacturing procedures of cemented carbide inserts, to improve their milling performance after a PVD coating deposition, Surf. Coat. Technol. 163 (2003) 625–630.

[26] U. Helmersson, M. Lattemann, J. Bohlmark, A.P. Ehiasarian, J.T. Gudmundsson, Ionized physical vapor deposition (IPVD): a review of technology and applications, Thin Solid Films 513 (2006) 1–24.

[27] Y.Y. Chang, D.Y. Wang, C.Y. Hung, Structural and mechanical properties of nano-layered TiAlN/CrN coatings synthesized by a cathodic arc deposition process, Surf. Coat. Technol. 200 (2005) 1702–1708.

[28] L. Zhan, A. Zhang, P. Héroux, X. Li, Z. Li, J. Zhao, Y. Guo, Y. Liu, Gasoline degradation and nitrogen fixation in soil by pulsed corona discharge plasma, Sci. Total Environ. 661 (2019) 266–275.

[29] G. Erkens, R. Cremer, T. Hamoudi, K.D. Bouzakis, I. Mirisidis, S. Hadjiyiannis, G. Skordaris, A. Asimakopoulos, S. Kombogiannis, J. Anastopoulos, K. Efstathiou, Properties and performance of high aluminum containing (Ti,Al)N based supernitride coatings in innovative cutting applications, Surf. Coat. Technol. 177 (2004) 727–734.

[30] J. Musil, Hard nanocomposite coatings: thermal stability, oxidation resistance and toughness, Surf. Coat. Technol. 207 (2012) 50–65.

[31] R. Messier, A.P. Giri, R.A. Roy, Revised structure zone model for thin film physical structure, J. Vac. Sci. Technol. A 2 (1984) 500–503.

[32] R. Boxman, Macroparticle contamination in cathodic arc coatings: generation, transport and control, Surf. Coat. Technol. 52 (1992) 39–50.

[33] D.B. Lewis, S.J. Creasey, C. Wüstefeld, A.P. Ehiasarian, P.Eh. Hovsepian, The role of the growth defects on the corrosion resistance of CrN/NbN superlattice coatings deposited at low temperatures, Thin Solid Films 503 (2006) 143–148.

[34] B. Warcholinski, A. Gilewicz, J. Ratajski, Z. Kuklinski, J. Rochowicz, An analysis of macroparticle-related defects on CrCN and CrN coatings in dependence of the substrate bias voltage, Vacuum 86 (2012) 1235–1239.

[35] M. Li, F. Wang, Effects of nitrogen partial pressure and pulse bias voltage on (Ti,Al) N coatings by arc ion plating, Surf. Coat. Technol. 167 (2003) 197–202.

[36] O. Favaron, M. Shi, Influence of bias voltage on properties of AlCrN coatings prepared by cathodic arc deposition, Surf. Coat. Technol. 224 (2013) 77–81.

[37] H. Willimann, P.H. Mayrhofer, L. Hultman, C. Mitterer, Hardness evolution of AlCrN coatings under thermal load, J. Mater. Res. 23 (2008) 2880–2885.

[38] E. Greene, J. Sundgren, L. Hultman, I. Petrov, Development of preferred orientation in polycrystalline TiN layers grown by ultrahigh vacuum reactive magnetron sputtering, Appl. Phys. Lett. 67 (1995) 2928–2930.

[39] J. Pelleg, L.Z. Zevin, S. Lungo, N. Croitoru, Reactive-sputter-deposited TiN films on glass substrates, Thin Solid Films 197 (1991) 117–128.

[40] Y.H. Cheng, T. Browne, B. Heckerman, Influence of CH$_4$ fraction on the

composition, structure, and internal stress of the TiCN coatings deposited by LAFAD technique, Vacuum 85 (2010) 89–94.

[41] R. Banerjee, R. Chandra, P. Ayyub, Influence of the sputtering gas on the preferred orientation of nanocrystalline titanium nitride thin films, Thin Solid Films 405 (2002) 64–72.

[42] J.E. Sundgren, Structure and properties of TiN coatings, Thin Solid Films 128 (1985) 21–44.

[43] P. Dubey, G. Martinez, S. Srivastava, R. Chandra, C.V. Ramana, Effect of bias induced microstructure on the mechanical properties of nanocrystalline zirconium tungsten nitride coatings, Surf. Coat. Technol. 313 (2017) 121–128.

[44] J. Lin, Z.L. Wu, X.H. Zhang, B. Mishra, J.J. Moore, W.D. Sproul, A comparative study of CrN$_x$ coatings synthesized by dc and pulsed dc magnetron sputtering, Thin Solid Films 517 (2009) 1887–1894.

[45] Y. Sun, Y.H. Wang, H.P. Seow, Effect of substrate material on phase evolution in reactively sputtered Cr-Al-N films, J. Mater. Sci. 39 (2004) 7369–7371.

[46] E.W. Niu, L. Li, G.H. Lv, H. Chen, W.R. Feng, S.H. Fan, S.Z. Yang, X.Z. Yang, Influence of substrate bias on the structure and properties of ZrN films deposited by cathodic vacuum arc, Mater. Sci. Eng. A 460 (2007) 135–139.

[47] J.A. Freeman, P.J. Kelly, G.T. West, J.W. Bradley, I. Iordanova, The effects of composition and pulsed biasing on chromium nitride films, Surf. Coat. Technol. 204 (2009) 907–910.

[48] R. Franz, J. Neidhardt, R. Kaindl, B. Sartoryb, R. Tessadrib, M. Lechthalerc, P. Polcikd, C. Mitterera, Influence of phase transition on the tribological performance of arc-evaporated AlCrVN hard coatings, Surf. Coat. Technol. 203 (2009) 1101–1105.

[49] H.S. Maharana, B. Bishoyi, A. Basu, Current density dependent microstructure and texture evolution and related effects on properties of electrodeposited Ni-Al coating, J. Alloys Compd. 787 (2019) 483–494.

[50] C. Wüstefeld, D. Rafaja, V. Klemm, C. Michotte, M. Kathrein, Effect of the aluminium content and the bias voltage on the microstructure formation in Ti$_{1-x}$Al$_x$N protective coatings grown by cathodic arc evaporation, Surf. Coat. Technol. 205 (2010) 1345–1349.

[51] L. Wang, S. Zhang, Z. Chen, J. Li, M. Li, Influence of deposition parameters on hard Cr-Al-N coatings deposited by multi-arc ion plating, Appl. Surf. Sci. 258 (2012) 3629–3636.

[52] A. Leyland, A. Matthews, On the significance of the H/E ratio in wear control: a nanocomposite coating approach to optimized tribological behavior, Wear 246 (2000) 1–11.

[53] N. Vidakis, A. Antoniadis, N. Bilalis, The VDI 3198 indentation test evaluation of a reliable qualitative control for layered compounds, J. Mater. Process. Technol. 143 (2003) 481–485.

[54] S. Zhang, D. Sun, Y. Fu, H. Du, Toughening of hard nanostructural thin films: a critical review, Surf. Coat. Technol. 198 (2005) 2–8.

[55] T. Banerjee, A.K. Chattopadhyay, Influence of substrate bias on structural and tribo-mechanical properties of pulsed magnetron sputtered TiN-WS$_x$ hard-lubricious coating, Tribol. Int. 123 (2018) 81–91.